



# Numerical and experimental investigation of magnesium/aluminum laser welding with magnetic field

Jiafu Zhou<sup>1</sup> · Dianwu Zhou<sup>1</sup> · Jinshui Liu<sup>1</sup>

Received: 8 March 2021 / Accepted: 11 June 2021 / Published online: 22 June 2021  
© The Author(s), under exclusive licence to Springer-Verlag London Ltd., part of Springer Nature 2021

## Abstract

A three-dimensional numerical model for thermal-fluid-metallurgical coupling was established to inspect the effect from a stable longitudinal magnetic field on molten pool of magnesium/aluminum laser welding. Magnetic field-assisted laser welding platform was built to test the morphology and spectrum of the metal vapor/plasma. The scanning electron microscope (SEM) and energy dispersive spectrometry (EDS) were used to determine the morphology and element distribution of molten pool cross section. Simulation results showed that temperature gradient of molten pool was reduced, heat distribution became uniform, and keyhole area was enlarged. In addition, the flow velocity of molten pool was increased, the vorticity of molten pool was improved, and the flow region of liquid metal was enlarged. Experimental results showed that penetration of molten pool was deeper, the shape of welding pool tended to be symmetrical, and the density of Al element distribution in welding pool was increased by magnetic field. Thus, heat and mass transfer in welding pool was promoted due to the application of magnetic field, the elements exchange and the convection of liquid metal were accelerated, and the distribution of Mg-Al compounds should be dispersed under the agitation of Lorentz force. It is predicted that the distribution of Mg-Al compounds in magnesium/aluminum laser welding would be positively affected by magnetic field, which was beneficial to control the weld quality. Hence, numerical results and experimental verification shared good consistency.

**Keywords** Laser fusion welding · Magnetic field · Magnesium-aluminum lap welding · Heat and mass transfer

## 1 Introduction

Mg alloys and Al alloys have been widely applied to aerospace and rail transportation industry for reducing structural weight, improving maneuverability, and reducing manufacturing costs. Therefore, it is inevitable for the connection between magnesium alloy and aluminum alloy. So far, laser beam welding has been used for Mg/Al connections. Liu et al. [1] carried out a laser welding experiment to bond AZ31B Mg alloy with A6061 Al alloy, and they reported that the reduction of intermetallic compounds was caused by the fluid from the gasification of the adhesive. Liu and Wang. [2] observed the microcracks of melting zone through scanning electron microscopy, and they discussed the influence of the

adhesive on the temperature distribution. Chang et al. [3] achieved laser-friction stir welding with an Ni foil filler, and they successfully increased the joint strength to 66% of the Mg metal tensile strength. Gao et al. [4] used fiber laser to join Mg and Al alloy with a Ti interlayer, and they found that the tensile strength was increased due to the suppression of Mg-Al compounds. Laser welding has its unique advantages, such as low heat input, small deformation, energy conservation, and high adaptability. However, as a kind of non-contact welding, laser welding can't make the welding pool be stirred effectively, which is detrimental to the heat and mass transfer and results in uneven distribution of molten metal composition and temperature. Several researchers tried to solve these problems in laser welding by adding magnetic fields. Tse et al. [5] discovered that magnetic support affected the screening efficacy of plasma on CO<sub>2</sub> laser welding, and the penetration depth of CO<sub>2</sub> laser was increased by 7%. R. Chen et al. [6] investigated magnetic field-stimulated laser-MIG combined jointing of 316 L steel and discovered that the magnetic field could improve the fatigue resistance and reduce the ferrite of the sample. Yan et al. [7] conducted laser beam welding of steel/aluminum with

✉ Dianwu Zhou  
hnu dwzhou@sina.com

<sup>1</sup> State Key Laboratory of Advanced Design and Manufacturing for Vehicle Body, Hunan University, Changsha, China

magnetic support and thought the magnetic support caused more iron-rich intermetallic compounds to be formed on the joint interface. Chen et al. [8] applied magnetic field-assisted fiber laser welding technique for joining 304 steel and declared that the magnetic field made the breadth of the transition area wider and improved the microstructure gradient of the weld seam. Qi et al. [9] performed magnetic field supported laser welding on 304 steel plate based on the observation on the formation of periodic roots with CCD, and they deduced that electromagnetic force can prevent periodic root humps. Zhu et al. [10] carried out laser wire filling welding on 316 L steel with constant magnetic field; they found that EMS refines the width of  $\gamma$  grains and promotes the uniformity of residual strain in the middle layer area while reducing the concentrated texture density. Xu et al. [11] performed full-penetration laser welding on A5083 aluminum alloy, and they concluded that appropriate oscillating electromagnetic field can effectively reduce the sagging of the weld root. Üstündağ et al. [12] conducted laser welding experiment on 25-mm-thick structural steel with an oscillating magnetic field, and they ascertained that the stability of the keyhole and the weld penetration depth were increased by magnetic field. Li et al. [13] applied electromagnetic-assisted wire wobbling in laser narrow gap welding of 316 L stainless steel, and they verified that the wettability of liquid weld metal on the sidewall of the groove was improved. Cao et al. [14] did magnetic field-assisted laser welding on a 2A12 aluminum alloy plate, and they pinpointed that the magnetic field can increase the depth and middle width of the weld bead. Liu et al. [15] fulfilled laser-MIG hybrid welding of 5052 aluminum alloy with magnetic field, and they discovered that the magnetic field can improve the stability of the keyhole, extend the solidification time of the molten pool, and provide more air bubbles escape channels. Chen et al. [16] investigated the weldability of medium-Mn nanostructured steel by external magnetic field-assisted laser welding, and they found that the grain size of the original austenite in the weld with an external magnetic field was more than twice finer than the grain size of the austenite in the laser weld without magnetic field. At the same time, some researchers have established numerical models and try to explain the unobservable data in laser welding with external magnetic fields. Gatzert and Tang. [17] set up a CFD-based pattern to calculate the velocity field of laser welding on aluminum alloy, and they found that the laser beam with stable magnetic field affects the direction of melt flow. Bachmann et al. [18] simulated the effect of a stable transverse magnetic field on high-power laser beam processing of Al alloy, and they believed the magnetic field altered the temperature distribution and eliminated the influence of thermo-capillary flow. Bachmann et al. [19] subsequently investigated the Hartmann effect of magnetic field on laser welding pool by building the model of magnetic field-assisted laser jointing of Al alloy, and they thought that it is advantageous for the uniform distribution of mechanical stress by

reducing the influence of Marangoni effect. Rong et al. [20] built a model of magnetic field supported laser welding of 316 L steel, and they suggested that magnetic field was helpful for reducing the welding deformation based on the calculated results. J. Chen et al. [21] established a magnetic field-assisted laser welding model for Al alloy plate, and they discovered that the thermal current was perpendicular to the solid/liquid line in the solid region and pointed to the centerline of the keyhole in the liquid region. However, until now, there was no report on numerical and experimental investigation of magnetic field-assisted Mg/Al laser welding.

In this paper, a three-dimensional numerical model for thermal-fluid-metallurgical coupling was established to calculate the temperature field, flow field, and electromagnetic field of the welding pond, and the electromagnetic field was directly introduced to obtain the data closer to the experiment. Magnetic field-assisted Mg/Al laser welding was carried out to verify the calculation results. The morphology and spectrum of the metal vapor/plasma were detected, the morphology and element distribution of the molten pool were characterized, and it was found that the numerical results and experimental verification share good consistency. Through this investigation, it was helpful to understand the influence of a stabilized magnetic field on Mg/Al laser fusion welding in order to control the weld quality.

## 2 Numerical simulation

The numerical simulations were performed using the commercial finite element solver COMSOL Multiphysics. A thermal-fluid-metallurgical coupling model of magnetic field-assisted magnesium/aluminum laser welding was established by considering the thermo-physical parameters of the metal liquid. Material parameters came from the material library of COMSOL Multiphysics are summarized in Table 1.

**Table 1** Material properties of Mg alloy AZ31 and Al alloy 6061 at melting temperature

Properties	Mg alloy AZ31	Al alloy 6061
Density ( $\text{kg}\cdot\text{m}^{-3}$ )	1780	2380
Thermal conductivity ( $\text{W}\cdot\text{m}^{-1}\cdot\text{K}^{-1}$ )	114	91
Specific heat ( $\text{J}\cdot\text{kg}^{-1}\cdot\text{K}^{-1}$ )	1413	1180
Dynamic viscosity (Pa·s)	$1.1 \times 10^{-3}$	$1.3 \times 10^{-3}$
Surface tension coefficient ( $\text{N}\cdot\text{m}^{-1}$ )	0.0256	0.871
Liquidus temperature (K)	923	933
Solidus temperature (K)	839	853
Reflectivity	0.7	0.8
Expansion coefficient ( $\text{K}^{-1}$ )	$2.957 \times 10^{-5}$	$2.547 \times 10^{-5}$
Electrical resistivity ( $\Omega\cdot\text{m}$ )	$19.18 \times 10^{-8}$	$24.77 \times 10^{-8}$

Different from the practice of adding Lorentz force as a volume force, the Lorentz force produced by a constant magnetic field was directly calculated in this model. As shown in Fig. 1, part of the weld is taken as calculation domain for analysis. The symmetrical calculation domain was set as the combination of a magnesium alloy AZ31 region (10 mm × 4 mm × 1.4 mm) and an aluminum alloy 6061 region (10 mm × 4 mm × 1.2 mm). Skewness is applied to characterize mesh quality, and its evaluation standard is listed in Fig. 2. The minimum mesh element quality was 0.1318, and the average mesh element quality was 0.6754. The planar Gaussian heat source was assumed to move along the centerline. Since the molten pool behavior in welding is a relatively complex transient process involving heat transfer, fluid dynamics, and electromagnetic, it is hard to simulate all physical phenomena; thus, the heat-flow-metallurgy coupling model was properly simplified. The basic settings of the model were as follows:

- The starting temperature was the same as the room temperature (293.15K).
- The molten pool motion state was assumed to be laminar flow. Boussinesq approximation was used to deal with the buoyancy term.
- Keyhole temperature was set to evaporation temperature.
- During the simulation, the pressure of the protective gas on the molten pool and the heat loss caused by the protective gas were ignored.
- On account of the powerfully heating from laser beam up to the metallic vaporization temperature, respondent heat caused by magnet system and formation heat generated from metal compounds forming were obliterate.
- The magnetic induction intensity of the stable longitudinal magnetic field was uniform.
- The loss of magnetic induction in the atmosphere was ignored.

### 2.1 Governing equations

The governing equations for heat source, mass, momentum, and energy conservation are given below, and the emulation framework of COMSOL Multiphysics was employed to put them into effect.

- Heat source equation:

$$Q(x, y) = \frac{2nP}{\pi r^2} e^{-\frac{2[(x-x_0)^2+(y-y_0)^2]}{r^2}} \tag{1}$$

Here,  $Q$  is the laser heat source,  $n$  is the absorption coefficient of laser beam,  $P$  is the laser power,  $r$  is the radius of laser spot, and  $x_0$  and  $y_0$  are coordinates of laser spot center.

- Mass conservation is expressed as:

$$\rho \nabla \cdot \mathbf{u} = 0 \tag{2}$$

Here,  $\rho$  represents the material density, and  $\mathbf{u}$  is the speed vector,  $\mathbf{u} = (u, v, w)$ .

- Momentum conservations are given as:

$$\rho \frac{\partial \mathbf{u}}{\partial t} + \rho(\mathbf{u} \cdot \nabla) \mathbf{u} = \nabla \cdot \left[ -p\mathbf{I} + \mu(\nabla \mathbf{u} + (\nabla \mathbf{u})^T) - \frac{2}{3} \mu(\nabla \cdot \mathbf{u})\mathbf{I} \right] + \mathbf{F} \tag{3}$$

$$\mathbf{F} = \mathbf{F}_{Buoyancy} + \mathbf{F}_{Lorenz} + \mathbf{F}_{Gravity} \tag{4}$$

Fig. 1 Computational domain and mesh for the calculations

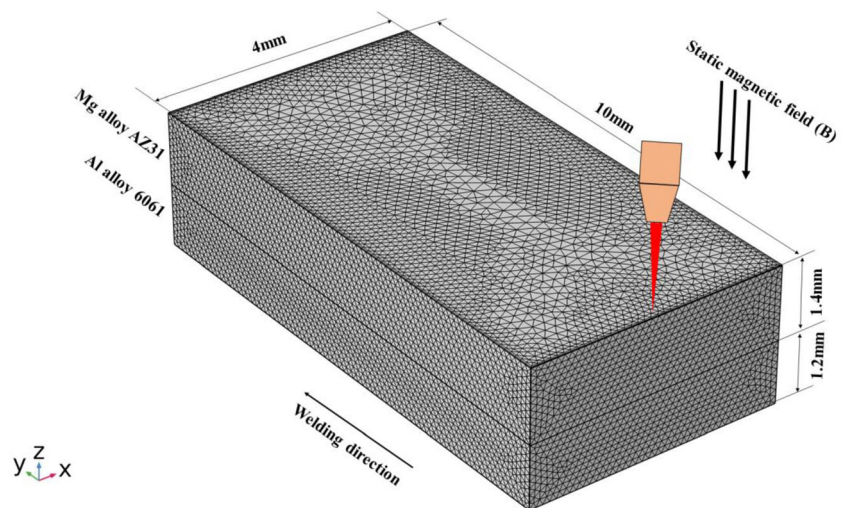


**Fig. 2** Evaluation standard of mesh element quality in skewness

0-0.25	0.25-0.50	0.50-0.80	0.80-0.95	0.95-0.98	0.98-1.00*
Excellent	very good	good	acceptable	bad	Inacceptable*

Here,  $\rho$  represents the density,  $T$  represents the temperature,  $t$  represents the welding time,  $p$  represents the pressure,  $\mu$  represents the viscosity, and  $F_{Buoyancy}$ ,  $F_{Lorentz}$ ,  $F_{Gravity}$  means the buoyancy force, the Lorentz force, and the gravity, respectively. Buoyancy caused by the expansion of molten metal is closely related to temperature. Buoyancy is expressed by Boussinesq approximation here:

$$F_{Buoyancy} = -\rho\beta(T-T_{melt})\mathbf{g} \tag{5}$$

where  $\beta$  is the thermal expansion coefficient,  $\mathbf{g}$  is the gravitational constant,  $T$  is the temperature, and  $T_{melt}$  is the melting point.  $F_{Lorentz}$  represents the Lorentz force caused by the extrinsic stable magnetic field and the movement of the conductive liquid.  $F_{Lorentz}$  is bewrited by the formulation below:

$$F_{Lorentz} = \mathbf{j} \times \mathbf{B} \tag{6}$$

Here,  $\mathbf{j}$  means the current density and  $\mathbf{B}$  means the magnetic induction intensity. The setting of current density and magnetic induction intensity will be mentioned later, and the expression of gravity is as follows:

$$F_{Gravity} = \rho\mathbf{g} \tag{7}$$

- Energy conservations are shown as:

$$\rho C_P \frac{\partial T}{\partial t} + \rho C_P \mathbf{u} \nabla T + \nabla \mathbf{q} = Q \tag{8}$$

$$\mathbf{q} = -\varphi \nabla T \tag{9}$$

where  $C_P$  is the constant pressure heat capacitance of material,  $\varphi$  is the thermal conductivity of material, and  $Q$  is the laser heat source.

- Electromagnetic field conservation equations are presented here:

$$\nabla \times \mathbf{H} = \mathbf{J} \tag{10}$$

$$\mathbf{B} = \nabla \times \mathbf{A} \tag{11}$$

$$\mathbf{J} = \sigma \mathbf{E} \tag{12}$$

$$\mathbf{E} = -\frac{\partial \mathbf{A}}{\partial t} \tag{13}$$

where  $\mathbf{H}$  connotes the magnetic field strength vector,  $\mathbf{J}$  connotes the current density,  $\mathbf{B}$  connotes the magnetic induction,  $\mathbf{A}$  connotes the magnetic vector potential,  $\sigma$  connotes the material conductivity, and  $\mathbf{E}$  connotes the electric field strength.

- Marangoni conservation equations: During welding, a molten pool is formed when the base metal reaches its own melting temperature. The Marangoni force affects the flow rate and temperature distribution, which can cause stress and deformation in the material. Marangoni conservation equations applied in the simulation are as follows:

$$\left[ -p\mathbf{I} + \mu \left( \nabla \mathbf{u} + (\nabla \mathbf{u})^T \right) - \frac{2}{3} \mu (\nabla \cdot \mathbf{u}) \mathbf{I} \right] \mathbf{n} = \gamma \nabla_t T \tag{14}$$

Here,  $T$  implies the temperature,  $p$  implies the pressure,  $\mu$  implies the dynamic viscosity of materials, and  $\gamma$  implies the surface tension.

- Seebeck effect conservation equations: Due to the Seebeck effect, a potential difference between the two materials is caused by the temperature difference between two different electrical conductors, so a thermal current is generated in the laser welding bath. Seebeck effect conservation equations used in the simulation are listed below:

$$\mathbf{q} = ST\mathbf{J} \tag{15}$$

$$\mathbf{J}_e = -\sigma S \nabla T \tag{16}$$

Here,  $S$  is the Seebeck coefficient of the material, provided by the material library.  $T$  is temperature, and  $\sigma$  is the material conductivity.

### 2.2 Boundary conditions

- Temperature field boundary conditions: considering the heat input and heat loss of the melting pool, the temperature field boundary condition equations are as follows:

$$-k \frac{\partial T}{\partial z} = Q - q_1 - q_2 \tag{17}$$

$$q_1 = h_1(T - T_0) \tag{18}$$

$$q_2 = \varepsilon\sigma_b(T^4 - T_0^4) \tag{19}$$

where  $k$ ,  $T$ ,  $q_1$ ,  $q_2$ ,  $h_1$ ,  $T_0$ ,  $\varepsilon$ , and  $\sigma_b$  refer to the thermal conductivity of the molten metal, the temperature, the convective heat loss on the metal face, the radiant heat loss when the laser acts on the material, the heat transfer coefficient of the weldment surface, the initial temperature, material surface reflectivity, and Stefan-Boltzmann constant, respectively.

- CFD boundary conditions: Taking the surface tension in the welding pond and the Marangoni force into consideration, Eqs. (20)–(22) show the equations of flow field boundary conditions for the simulations.

$$\mathbf{u} \cdot \mathbf{n} = 0 \tag{20}$$

$$-\mu \frac{\partial u}{\partial z} = \frac{\partial \gamma}{\partial T} \frac{\partial T}{\partial x} \tag{21}$$

$$-\mu \frac{\partial v}{\partial z} = \frac{\partial \gamma}{\partial T} \frac{\partial T}{\partial y} \tag{22}$$

Here,  $\mu$  is the viscosity, and  $\gamma$  is the surface tension. Equations (21) and (22) were used for the top boundary; Eq. (20) was used for other boundaries.

- Electromagnetic field boundary conditions: The area of magnetic field was set near the molten pool for the purpose of reducing simulation workload. The electromagnetic fields were isolated from all other air boundaries. The boundary condition formulations are as follows:

$$\mathbf{n} \times \mathbf{A} = 0 \tag{23}$$

$$\mathbf{n} \times \mathbf{B} = 0 \tag{24}$$

where  $\mathbf{n}$  means the normal vector on the outsides,  $\mathbf{B}$  is the magnetic induction vector, and  $\mathbf{A}$  is the vector magnetic vector potential.

### 3 Experimental procedure

A stable longitudinal magnetic field-assisted laser welding platform was built. The fiber laser IPG-YLS-5000 with 0.4-mm minimum spot diameter and 1.07  $\mu\text{m}$  wavelength was applied. A three-dimensional five-axis laser machine tool was used to control the welding path. The materials were

Mg alloy AZ31 (100 mm  $\times$  30 mm  $\times$  1.4 mm) and Al alloy 6061(100 mm  $\times$  30 mm  $\times$  1.2 mm). The chemical components of AZ31 and 6061 are illustrated in Table 2. The welding experiment scheme and experimental platform are shown in Figs. 3 and 4, separately. The laser beam was incident on the metal sheet at an angle of 20° to the vertical direction. The power of laser beam was 1400 W and defocus distance was set to 0. The welding velocity was set to 1500 mm/min. The shielding gas was high-purity argon gas at an angle of 45° to the welding direction, and its flow rate was 1.5m<sup>3</sup>/h. Magnetic field was supplied by Nd<sub>2</sub>Fe<sub>14</sub>B magnets below the weld puddle, and magnetic induction intensity for the weld was adjusted by changing the number of magnets. The magnetic induction intensity was measured via a HT20 Tesla meter. A MEMRECAM HX-6e high-speed video camera was applied to seize the metal vapor/plasma topography above the molten pool, while a microspectrometer Ocean HR2000+ was matched to detect the metal vapor/plasma spectral. After welding, the cross-sectional morphology of welding pond and the distribution of compounds in welding pond were inspected by using a scanning electron microscope (SEM) with an energy dispersive spectrometry (EDS) probe.

### 4 Numerical results and analysis

In this section, the numerical results of magnesium/aluminum laser welding with/without magnetic field were presented.

#### 4.1 No magnetic field-assisted case

The temperature distribution and the velocity vectors of the molten pond along the welding path for the reference case are displayed in Fig. 5. When no magnetic field was added, the keyhole area was small, the temperature field gradient of the molten pool was large, and center temperature differed greatly from the surrounding temperature in the welding pool. Flow velocity of metal liquid was very low. The velocity distribution was further analyzed. The main flowing routine of the molten metal is marked with black arrows in Fig. 5a. At the surface, the liquid metal flowed from the hot center area around the keyhole to the weld pool boundary that maintained the melting temperature. Therefore, the weld pool stretched at the surface. The vorticity streamlines were disordered,

**Table 2** Chemical component (Wt%) of Mg alloy AZ31 and Al alloy 6061

Alloy	Mg	Si	Cu	Cr	Zn	Mn	Al	Ca
AZ31	Bal.	0.08	0.01	–	0.98	0.55	3.5	0.04
6061	1.1	0.7	0.35	0.25	0.25	0.15	Bal.	–

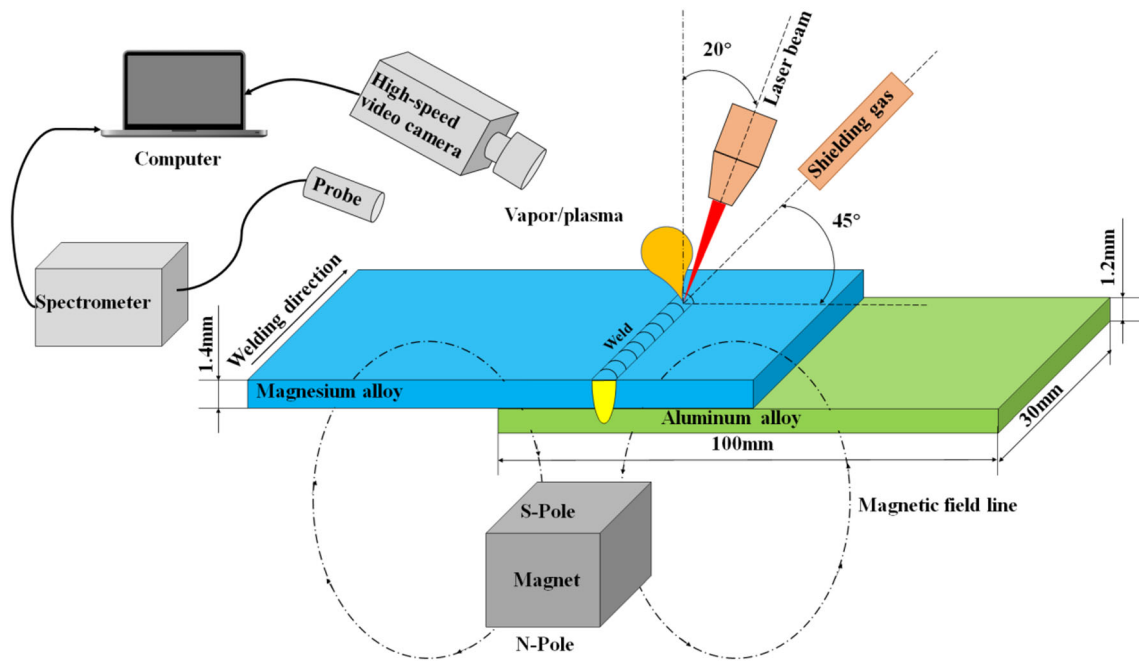
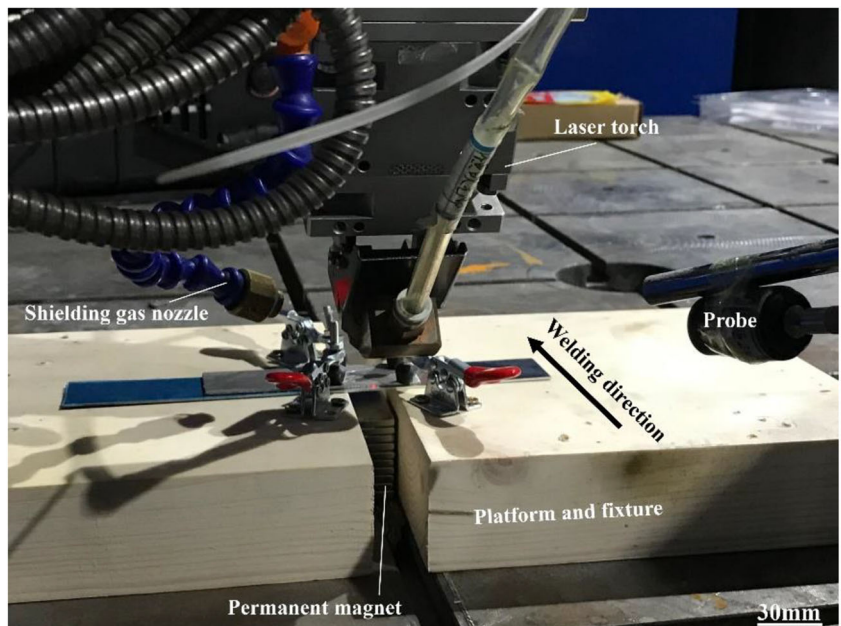


Fig. 3 Magnetic field-assisted laser welding scheme

indicating that there was no regular rotation in the molten pool nor visible mixing effect. In general, the flow performance of the melted metal was mainly affected by the Marangoni convection due to surface tension forces created by the surface tension gradient on the basis of the research of Fuhrich et al. [22]. Furthermore, surface tension gradient would drive the fluid to flow towards the regions with higher surface tension, which directly came from the influence of the temperature gradient according to the report of Mills et al.

[23]. As a kind of non-contact welding, liquid flow of laser welding pool was chiefly affected by Marangoni convection effect, recoil pressure, and buoyancy force. Accordingly, the fluid velocity was relatively low, and the energy from the heat source was hard to be diffused in melting pool. It could be known from Fig. 5 that the temperature gradient at the front end is higher than the temperature gradient at the back end in welding pool and the surface tension in front of the welding pool was greater.

Fig. 4 Experimental platform



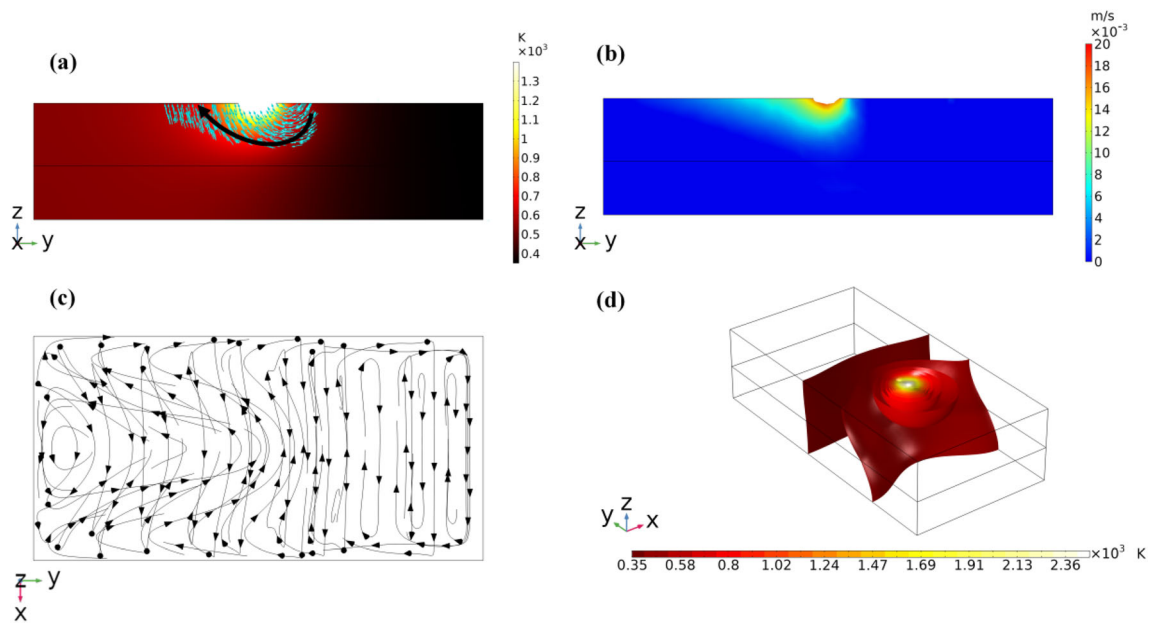


**Fig. 5** Reference case with no magnetic assistance. (a) Temperature distribution and velocity vectors. (b) Velocity distribution. (c) Vorticity streamlines of the whole calculation domain in top view. (d) Isothermal surface distribution up to the heat source center

### 4.2 Magnetic field-assisted cases

Figure 6 displays the results of the simulations with 150 mT steady magnetic field applied. It was discovered that the keyhole area was enlarged, and the temperature gradient of the welding pond was lessened. The subsurface of the temperature field was semi-ellipsoidal as a whole, and the area of thermal surface was relatively more uniform overall. The flow field distribution was also analyzed. It could be seen that the flow

velocity of the welding pool was increased. The main flowing routine of the liquid alloy is shown by black arrows in Fig. 6a. As laser heat source moved, the molten alloy first flowed around the keyhole and continued to flow backwards along the side of the molten pool according to the velocity vectors and distribution. The vorticity streamlines illustrated that a regular rotation was produced around the heat source. Moreover, the flow region of liquid metal was larger, which suggests the penetration of molten pool would be deeper.

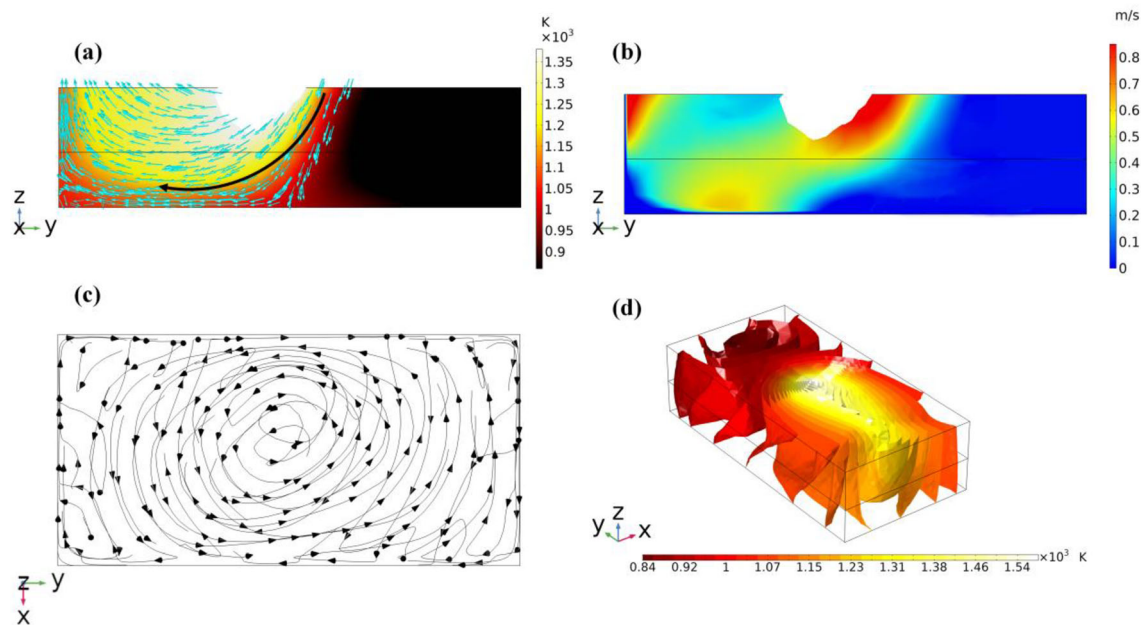


**Fig. 6** Magnetic field-assisted case. (a) Temperature distribution and velocity vectors. (b) Velocity distribution. (c) Vorticity streamlines of the whole calculation domain in top view. (d) Isothermal surface distribution up to the heat source center

The distribution of the current and Lorentz force is shown in Fig. 7. According to the Seebeck effect, if the temperatures of the two contact points in a circuit composed of two metals are different, electrons will shift along temperature gradient and accumulate so that thermal current appears. When two metals are in contact, there will be a contact potential difference, which depends on the electron spillover work and the difference in electron concentration. In the laser welding pool, liquid metal and the base metal could be regarded as two different metals, and the temperature difference was large. Therefore, there was a certain intensity of thermal current in melting pond during the laser welding procedure. The molten pool could be regarded as the inside of a battery, the high-temperature region was the positive electrode, and the low-temperature region was the negative electrode, so the thermal current in welding pool was directed from the low-temperature region to the high-temperature region. On the basis of Seebeck effect conservation equations, the original current in the molten pool was expressed as:

$$\mathbf{J}_{original} = \sigma \left( \frac{1}{e} \nabla \mu + S \nabla T \right) \quad (25)$$

Here,  $\mathbf{J}$  was the current density,  $\sigma$  was the conductivity of metal,  $e$  was the charged value per unit charge,  $S$  was the Seebeck coefficient, and  $\mu$  was the chemical potential of the metal.

Since the current value generated by the chemical potential in molten pool was small, it could be ignored. Thus, Eq. (25) was rewritten as:

$$\mathbf{J}_{original} \approx \mathbf{J}_{thermal} = \sigma S \nabla T \quad (26)$$

Based on the phenomenon of electromagnetic induction, an induced current would be generated in the conductor if a part of the conductor of the closed circuit performed cutting

magnetic induction motion. When magnetic field was added, magnetic field lines were cut by the flow of liquid metal in molten pool, and an induced current was generated in the workpiece, and the induced current would hinder the thermal current in molten pool according to Lenz's law. Thus, induced current could be presented as:

$$\mathbf{J}_{induced} = \sigma \mathbf{u} \times \mathbf{B} \quad (27)$$

Here,  $\sigma$  was the conductivity of metal,  $\mathbf{u}$  was the speed vector of metal liquid, and  $\mathbf{B}$  was magnetic induction intensity.

Based on Eq. (26) and Eq. (27), total current density in molten pool could be expressed by Eq. (28), and the total current in the molten pool shall be less than the thermal current due to the obstruction of the induced current.

$$\mathbf{J}_{total} = \sigma (\mathbf{u} \times \mathbf{B} + S \nabla T) \quad (28)$$

Further analysis is made in Fig. 8. In view of Zhang et al. [24], the metal flowing up and down parallel to the magnetic field lines would not be affected by the Lorentz force. Since the current in the  $Z$ -axis direction was parallel to the direction of the stable magnetic field and would not contribute to the production of the Lorentz force, only the current densities in the  $X$ -axis and  $Y$ -axis directions were integrated. It could be seen that the difference between the integral curve of the total current and the thermal current was very small since the induced current was generally weaker than the thermal current, so the magnitude of the total current and the thermal current was nearly the same. Although the direction of the total current was affected by the induced current, the total current generally pointed from the low-temperature area to the high-temperature area, which was similar to the direction of thermal current. The Lorentz force produced from the magnetic field and electric current tended to penetrate the interface of molten pool, which was helpful for the convection of liquid metal and

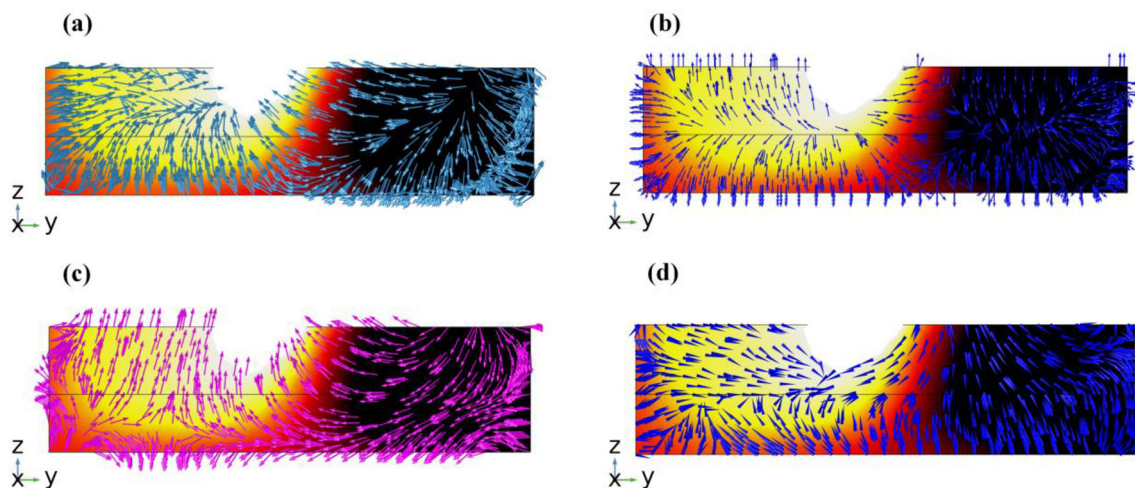
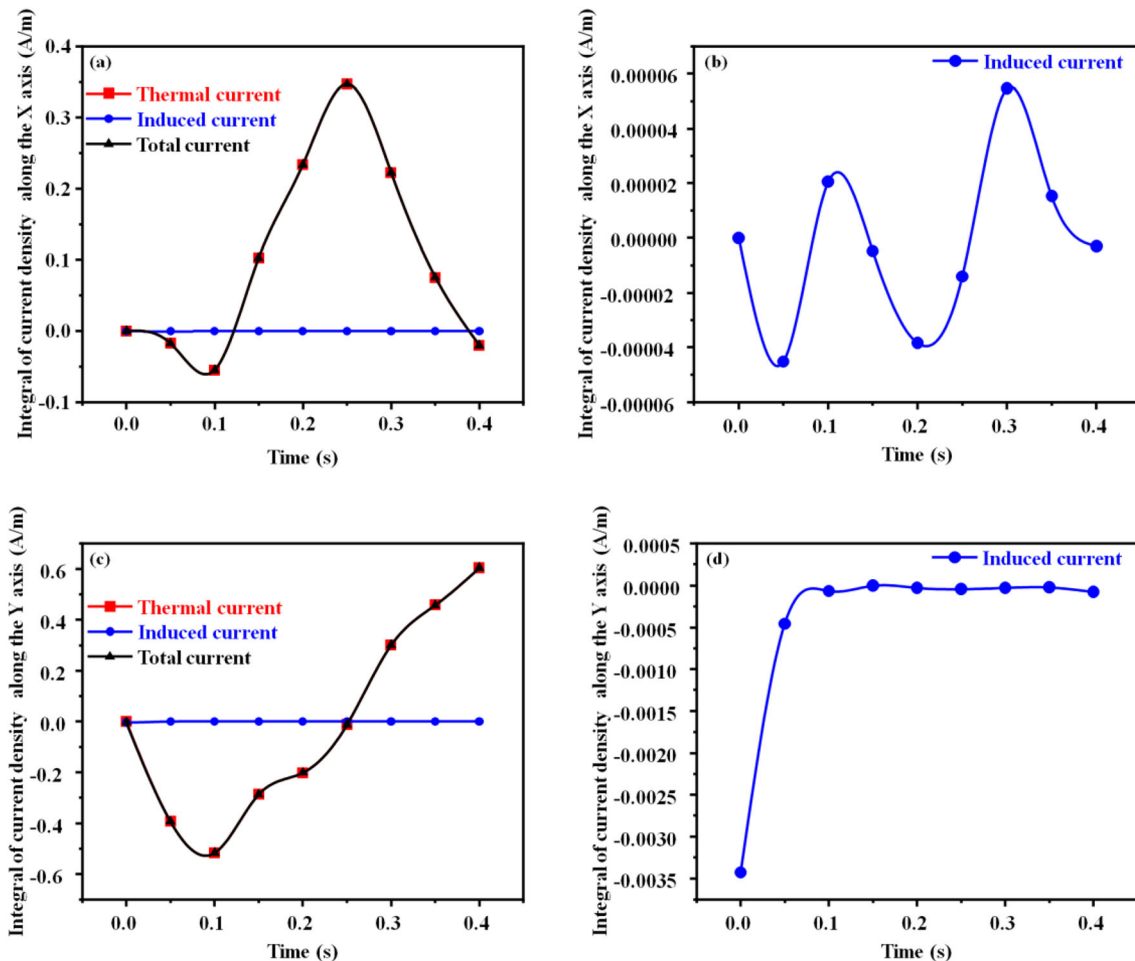


Fig. 7 Distribution of the current and Lorentz force: (a) thermal current, (b) induced current, (c) total current, (d) Lorentz force





**Fig. 8** Comparison of the integral of current density in  $X$ -axis and  $Y$ -axis: (a)(b) integral of current density in  $X$ -axis; (c)(d) integral of current density in  $Y$ -axis

the prevention for continuous distribution of brittle Mg-Al intermetallic compounds (Mg-Al IMC) at the interface of molten pool. This calculation showed that mixing effect occurred in the molten pool under the intention of a magnetic field. Thus, the heat and mass transfer process in the molten pool would be promoted. Moreover, it can be inferred that the penetration depth would be increased, and the defects (such as cracks and pores) of molten pool shall be decreased, leading to better weld quality.

Figure 9 exhibits the temperature gradient and heat flux of the weld pool. It could be learned that the temperature gradient curve without magnetic support was obviously above that with magnetic support. Usually, instant heat flux was used to represent heat transfer efficiency. It was apparent that instant heat flux in the melting pool at  $B = 0$  mT was much smaller than that of  $B = 150$  mT. The molten pool was agitated by Lorentz force, and heat diffused with the activity of liquid alloy in the magnetic pond. Thus, it could be seen that heat transfer efficiency of the welding pond was improved by magnetic field.

Figure 10 shows the Reynolds number and vorticity magnitude, which were meaningfully improved when magnetic field was added. A rotating motion of the molten metal aroused by the mixing action of the magnetic field was generated; thus, the flow rate was accelerated, and the vortex intensity was increased. Based on analysis on the calculation results of temperature and velocity distribution, it could be inferred that the heat transfer and mass transfer processes in welding pool were promoted because of the mixing effect of magnetic field.

## 5 Experimental results and analysis

### 5.1 Test results during welding

#### 5.1.1 High-speed camera shooting results

In this section, metal vapor/plasma topography at 3 mm above the molten pool was analyzed for the longitudinal magnetic fields of 0 mT and 150 mT. In the process of shooting, frames

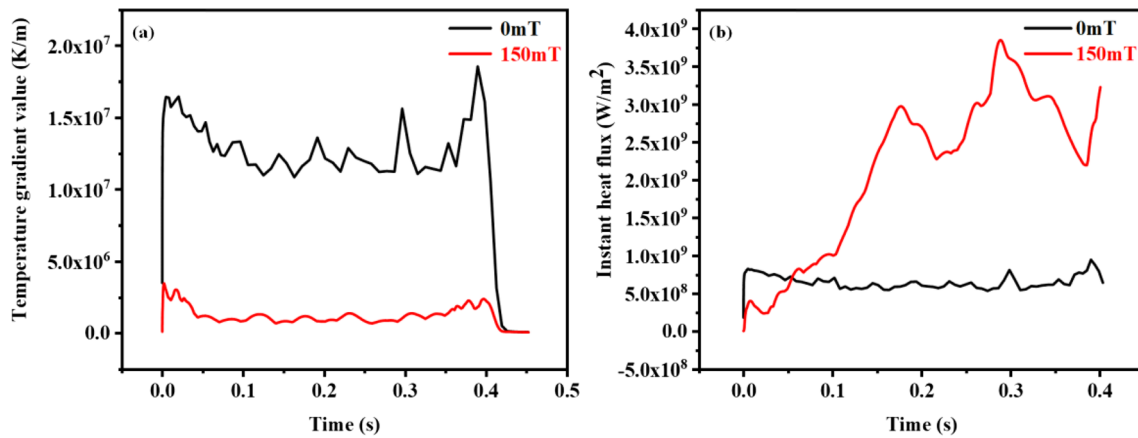


Fig. 9 Contrast of temperature gradient (a) and instant heat flux (b)

per second (FPS) of the high-speed camera was set to 2000. Since the test acquisition was presented as video, the shape acquired by the time period of 403.3–405.4 ms was finally selected for analysis, and the time interval was 0.2 ms. The results are shown in Fig. 11.

Since metal vapor/plasma exhibited periodicity during laser welding, when metal vapor/plasma increased to a certain amount, laser energy was shielded to a certain extent; metal vapor became dark and was dispersed. When  $B$  was equal to 0 mT, it could be seen that metal vapor/plasma above the molten pool was weak, the morphology density was small, and the brightness was relatively low. When  $B$  was equal to 150 mT, vapor/plasma was thicker than that of 0 mT. Meanwhile, the brightness was higher, and the total amount was relatively larger.

According to the photography, it may be seized that the appearance grew thicker and the overall brightness got higher as the magnetic induction intensity increased. The liquid metal in molten pool was more likely to evaporate in the form of metal vapor owing to the promotion of heat transfer in laser welding pool caused by magnetic support. In addition, the mixing feather upon the molten pool tended to extend and

diffuse when magnetic field was applied, leading to the bulk dilatation and denseness decrease of the laser-prompted plasma. Therefore, the shielding effects such as scattering, reflecting, and absorbing of the vapor/plasma on the laser beam would be correspondingly reduced, and more optical energy was illuminated upon the metal. In consequence, more metal vapor would be produced through further laser-vapor interactions, and more plasma would be generated, too. These laser-vapor interactions will be expanded under the lead of magnetic field according to the research on vapor/plasma of Z.Wang et al. [25] and H.Wang et al. [26], which were in good agreement with our experimental results. Besides, Huang et al. [27] also mentioned that magnetic field was beneficial to keep plasma plume staying above the welding pool. So, the total amount of metal vapor/plasma would be increased with the introduction of magnetic field.

### 5.1.2 Spectral detection result

Figure 12 exhibits metal vapor/plasma spectral comparison. Here, the band was in the range of 375 nm–395 nm, the largest relative intensity of the element spectrum appeared at 383.83

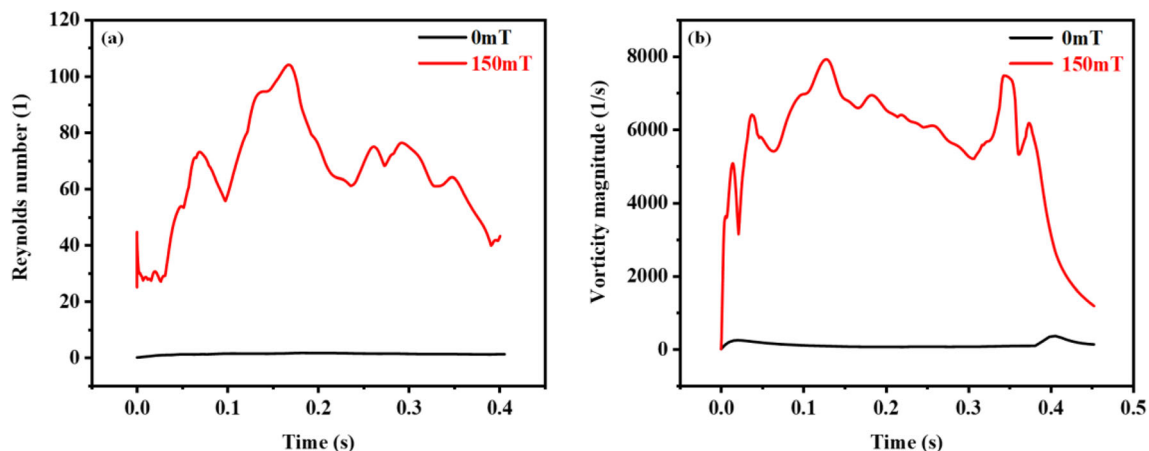
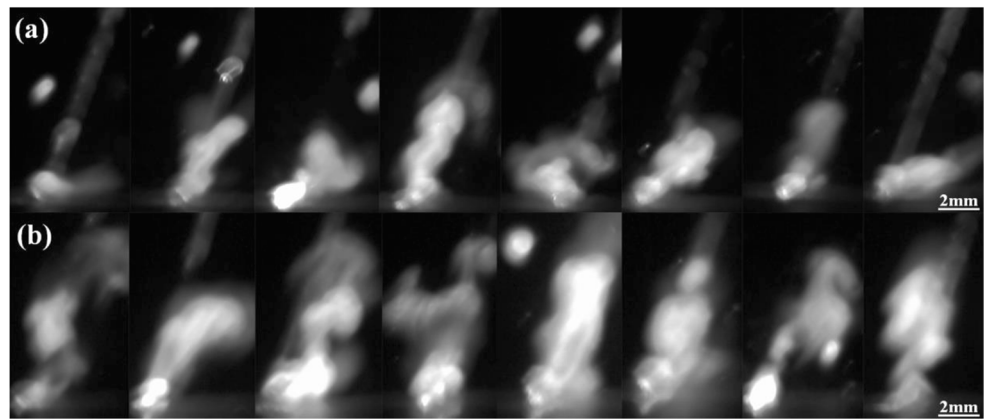


Fig. 10 Comparison of unit Reynolds numbers (a) and vorticity magnitude (b)

**Fig. 11** Metal vapor/plasma topography: (a)  $B = 0$  mT. (b)  $B = 150$  mT



nm, and the element represented by this point was the Mg element according to the NIST Atomic Spectra Database Lines Form. The Mg spectral intensities at 0 mT and 150 mT were 5130.39 and 6831.67, respectively. After Lorentz fitting and calculation, the electron density of the metal vapor/plasma at 0 mT and 150 mT was  $4.59 \times 10^{15} \text{ cm}^{-3}$  and  $4.86 \times 10^{15} \text{ cm}^{-3}$ , respectively. Usually, the electron denseness of the metal vapor/plasma represents the density of the metal vapor/plasma particles. These results suggested that the total amount of metal vapor/plasma in the region above the welding pond was enhanced by magnetic field. That means, when metal plate absorbed more laser energy with the magnetic support, more metal melted and ablated, resulting in more Mg particles escaping from the weld.

## 5.2 Test results after welding

### 5.2.1 SEM test results

The shape of the molten pool is displayed in Fig. 13. In the case without magnetic field, the curvature difference was large between two sides of the molten pool. Some cracks were

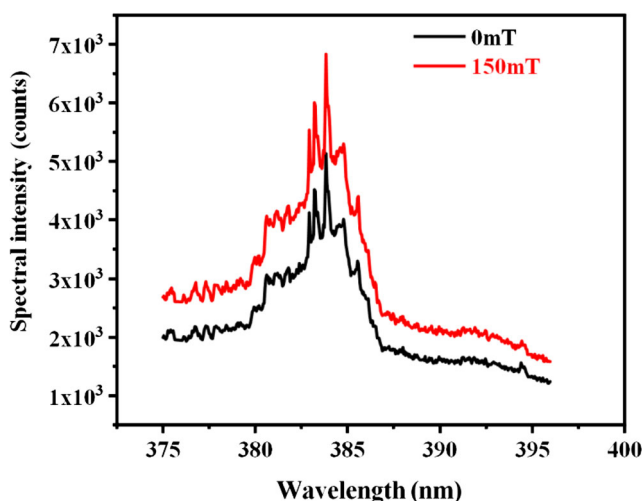


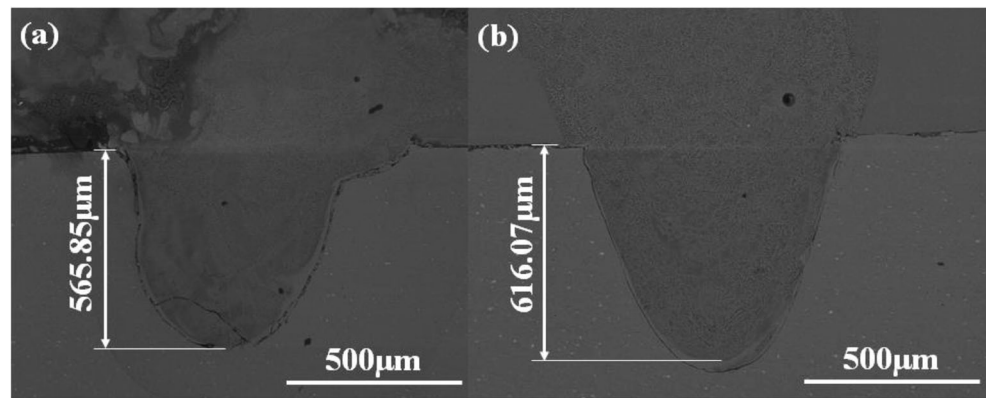
**Fig. 12** Metal vapor/plasma spectral comparison

formed inside the molten pool, and they were mainly distributed in the heat-affected zone around the molten pool. There were a few pores in the lower part of the molten pool, and the penetration depth on aluminum was  $565.85 \mu\text{m}$ . While a longitudinal magnetic field of 150 mT was introduced, the sides of the molten pool were basically symmetrical, and the curvatures of two sides were approximately the same. Meanwhile, the visible pores and cracks around the molten pool were also reduced, and the penetration depth on aluminum reached  $616.07 \mu\text{m}$ . With the introduction of magnetic field, the depth of the welding pond became deeper, the sides of the welding pond became more symmetrical, and the pores and cracks were less. Usually, the Mg/Al elements do not have time to diffuse during laser lap welding because of the rapid cooling process and the density difference between Mg/Al. Therefore, brittle Mg-Al IMC are usually continuously distributed at the interface, thereby reducing welding quality. As inferred before, Lorentz force tended to penetrate the interface of molten pool, brittle Mg-Al IMC should be dispersed by Lorentz force and was hard to enrich at the interface, resulting in better weld quality. Therefore, simulation results and SEM test results showed a good agreement.

### 5.2.2 EDS test results

Figure 14 shows the line scan results of magnesium/aluminum laser welding pool with and without magnetic field. Considering the way of lap welding on Mg/Al, the main element in the molten pool should be Mg, so the distribution of Al in the molten pool can be used to characterize the mixing in the molten pool. It could be seen that the Al element fluctuation amplitude with magnetic support was obviously lower than that without magnetic field. Figure 15 shows surface scanning results of welding pool with and without magnetic field. It could be observed intuitively that the density of Al element distribution in the 150 mT molten pool was higher than that of 0 mT molten pool, which implies that the magnetic field promoted element exchange and convection of liquid metal in the molten pool. These results suggest that better

**Fig. 13** Comparison of the shape of the molten pool: (a)  $B = 0$  mT, (b)  $B = 150$  mT



magnesium/aluminum weld quality would be obtained under the mixing effect caused by the longitudinal magnetic field, which was proved in Fig. 13. The results of EDS test were identical with the simulation results in terms of whether the magnetic field promoted the mass transfer procedure in the welding pool.

As shown in Fig. 16, there exists thermal current in the welding pool caused by the Seebeck effect. After the application of magnetic field, an induced current is generated from the movement of metal liquid. Since the induced current is much weaker than the thermal current, the magnitude of total current is almost the same as that of the thermal current, but the direction differs. Molten metal is driven to rotate by the Lorentz force in a stable magnetic field with the two kinds of currents; thus, a mixing effect is formed. In consequence, the

spread of heat in the molten pool is broadened (Figs. 5a and 6a), the temperature gradient is decreased (Figs. 5d, 6d, and 9a), and the instant heat flux of the pool rises (Fig. 9b), making heat transfer promoted in molten pool. Moreover, the shielding effect of the vapor/plasma on the laser beam is reduced by magnetic field, and the weld will assimilate more laser energy, bringing about more metal ablation and more production of metal vapor/plasma in the welding pool (Fig. 11). Meanwhile, the flow velocity of the molten metal becomes higher (Figs. 5b and 6b), the flow region of liquid metal was larger (Figs. 5a and 6a), and the vorticity magnitude of the pool becomes stronger (Figs. 5c and 6c) under the mixing effect by adding magnetic field, which accelerates the mixing process of liquid metal and element exchange in the pool. Consequently, the shape of welding pool tended to be

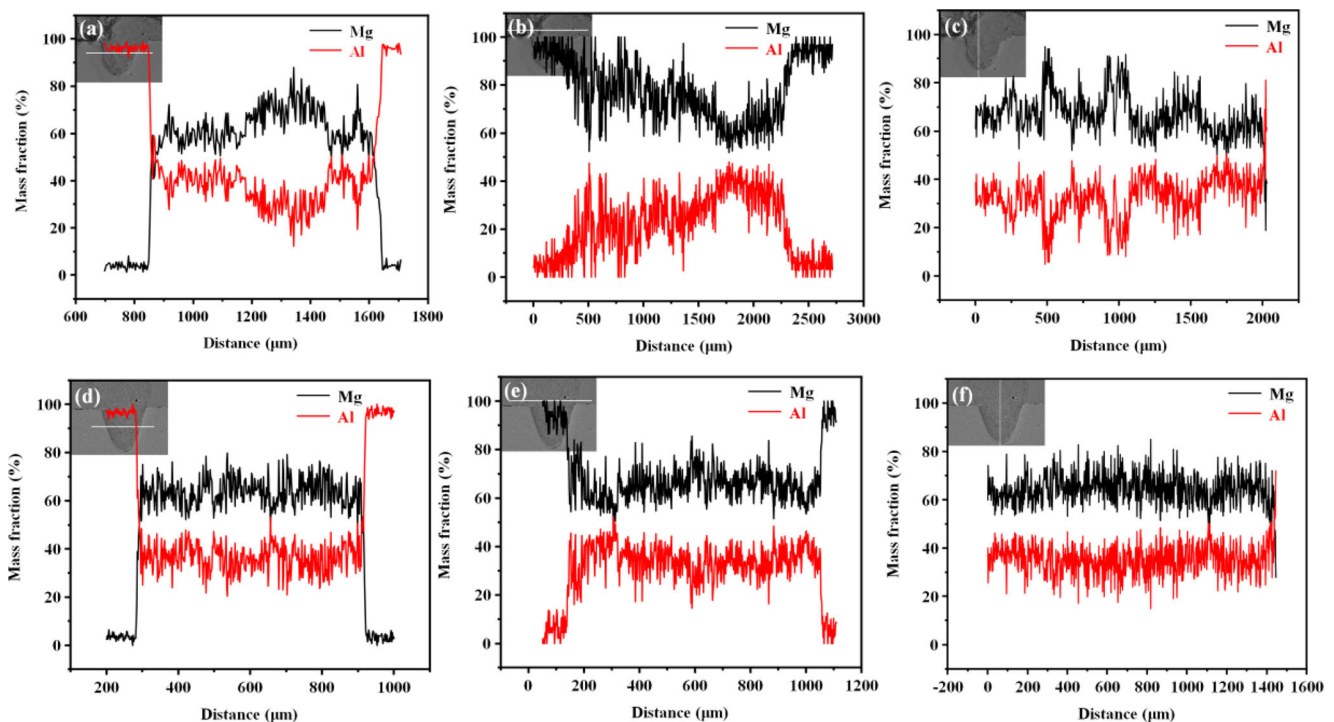
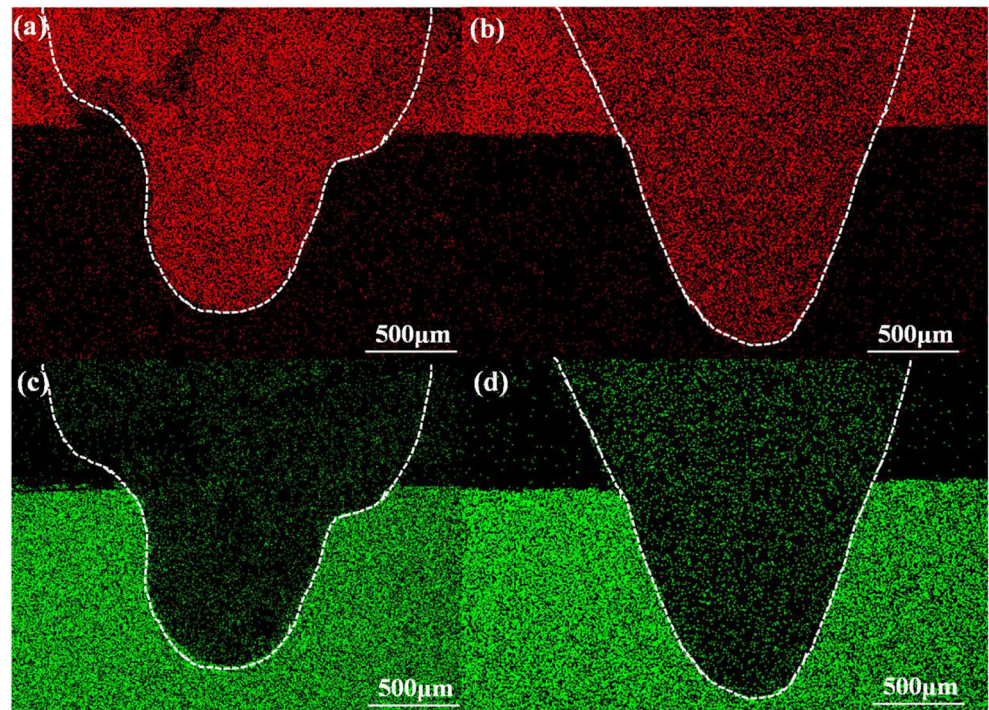


**Fig. 14** Comparison of the line scan position and results: (a) (b) (c) from  $B = 0$  mT, (d) (e) (f) from  $B = 150$  mT

**Fig. 15** Comparison of surface scan: Surface scan results of magnesium when (a)  $B = 0$  mT, (b)  $B = 150$  mT, and surface scan results of aluminum when (c)  $B = 0$  mT, (d)  $B = 150$  mT



symmetrical, the penetration of molten pool became deeper (Fig. 13), and the density of Al element distribution in molten pool was increased (Figs. 14 and 15). Generally, without the applied magnetic field, Mg and Al have no time to diffuse to the molten pool due to the rapid solidification of laser welding. Thus, brittle Mg-Al compounds are continuously distributed at the interface, resulting in some defects (such as crack) in the welded joint (Fig. 13a). Combined with the numerical results and experimental verification, it is predicted

that fragile Mg-Al compounds should be dispersed under the agitation from Lorentz force (Fig. 7d), so the defects of the welded joint were reduced (Fig. 13b), resulting in better weld quality. On the one hand, the flow direction of the liquid metal in molten pool will be changed under the Lorentz force. On the other hand, the current in the metal will also be changed as a result of the motion of the molten metal, which makes the Lorentz force altered. Based on the above analysis, it can be thought that the heat and mass transfer process in the molten

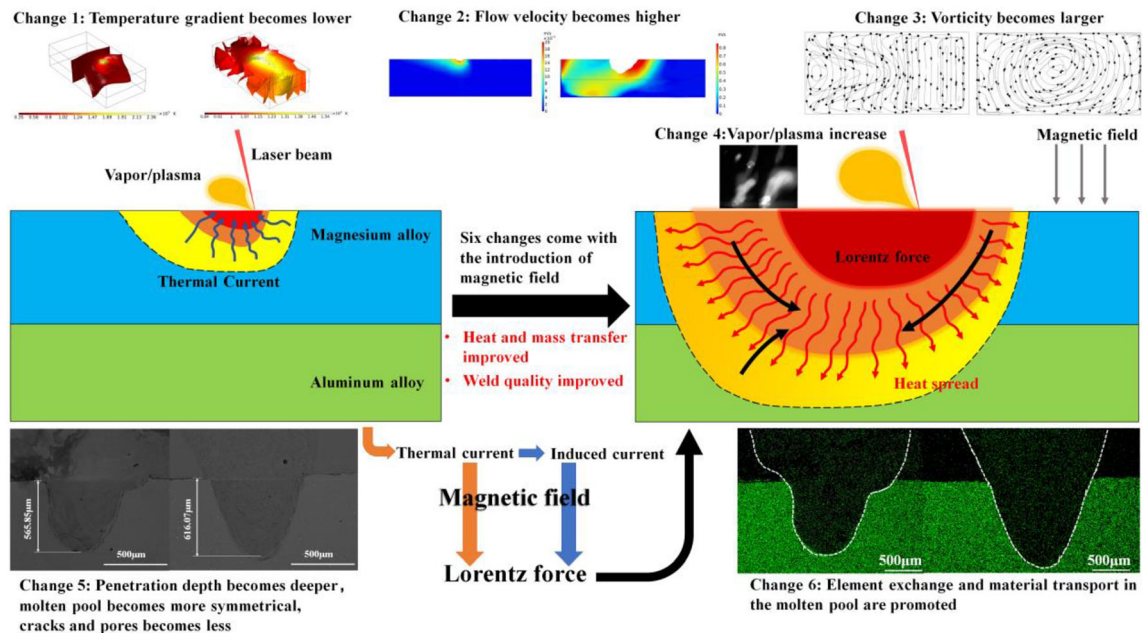


**Fig. 16** Schematic diagram of the longitudinal magnetic field mixing the molten pool

pool and weld quality are improved by the mixing effect from 150 mT magnetic field on magnesium/aluminum laser welding.

## 6 Conclusions

In this paper, numerical and experimental inspections of magnesium/aluminum laser welding with magnetic field were carried out, and the following conclusions were obtained.

- (1) According to simulation results, it was found that temperature field gradient of molten pool was reduced, heat distribution was uniform, and keyhole area was enlarged, which means heat transfer of molten pool was promoted by magnetic field. In addition, flow velocity of molten pool was increased, the flow region of liquid metal was enlarged, and the vorticity of molten pool was improved by Lorentz force; thus, mass transfer in molten pool was also promoted.
- (2) Based on experiment results, it was helpful for magnetic field to lessen the shielding effect of vapor/plasma. As magnetic field was introduced, the penetration of molten pool became deeper, the shape of molten pool became symmetrical, and some defects, such as pores and cracks, were reduced. Moreover, the density of Al element distribution in molten pool was increased by magnetic field, which means the material transport was boosted in molten pool.
- (3) Numerical results and experimental verification shared good consistency. Heat and mass transfer in welding pool was promoted due to the application of magnetic field; the elements exchange and convection of liquid were accelerated by Lorentz force; thus, the distribution of Mg–Al compounds shall be dispersed under the action of Lorentz force, which was favorable to control the weld quality.

**Availability of data and material** All data generated or analyzed during this study are included in the manuscript.

**Code availability** Not applicable.

**Author contribution** **Jiafu Zhou:** Data curation, writing-original draft, software, visualization, investigation

**Dianwu Zhou:** Conceptualization, methodology, writing-review and editing

**Jinshui Liu:** Supervision

**Funding** The authors received financial support from the National Key Research and Development Project of China (No. 2018YFB1107905) and the National Natural Science Foundation of China (51674112).

## Declarations

**Ethics approval** Not applicable.

**Consent to participate** Not applicable. The article involves no studies on humans.

**Consent for publication** Not applicable. The article involves no studies on humans.

**Competing interests** The authors declare no competing interests.

## References

1. Liu LM, Wang HY, Zhang ZD (2007) The analysis of laser weld bonding of Al alloy to Mg alloy. *Scr Mater* 56:473–476. <https://doi.org/10.1016/j.scriptamat.2006.11.034>
2. Liu LM, Wang HY (2009) The effect of the adhesive on the microcracks in the laser welded bonding Mg to Al joint. *Mater Sci Eng A* 507:22–28. <https://doi.org/10.1016/j.msea.2008.11.061>
3. Chang WS, Rajesh SR, Chun CK, Kim HJ (2011) Microstructure and mechanical properties of hybrid laser-friction stir welding between AA6061-T6 Al alloy and AZ31 Mg alloy. *J Mater Sci Technol* 27:199–204. [https://doi.org/10.1016/S1005-0302\(11\)60049-2](https://doi.org/10.1016/S1005-0302(11)60049-2)
4. Gao M, Mei S, Li X, Zeng X (2012) Characterization and formation mechanism of laser-welded Mg and Al alloys using Ti interlayer. *Scr Mater* 67:193–196. <https://doi.org/10.1016/j.scriptamat.2012.04.015>
5. Tse H, Man H, Yue T (1999) Effect of magnetic field on plasma control during CO<sub>2</sub> laser welding. *Opt Laser Technol* 31:363–368. [https://doi.org/10.1016/S0030-3992\(99\)00080-8](https://doi.org/10.1016/S0030-3992(99)00080-8)
6. Chen R, Jiang P, Shao X, Mi G, Wang C (2018) Enhancement of fatigue resistance for 316L welds produced by magnetic field assisted laser-MIG hybrid welding. *J Mater Process Technol* 254: 114–123. <https://doi.org/10.1016/j.jmatprotec.2017.11.030>
7. Yan F, Wang X, Chai F, Ma H, Tian L, Du X, Wang C, Wang W (2019) Improvement of microstructure and performance for steel/Al welds produced by magnetic field assisted laser welding. *Opt Laser Technol* 113:164–170. <https://doi.org/10.1016/j.optlastec.2018.12.030>
8. Chen X, Luo M, Hu R, Li R, Liang L, Pang S (2019) Thermo-electromagnetic effect on weld microstructure in magnetically assisted laser welding of austenite steel. *J Manuf Process* 41:111–118. <https://doi.org/10.1016/j.jmapro.2019.03.033>
9. Qi Y, Chen G, Deng S, Zhou D (2019) Periodic root humps in thick-plate laser welding using steady electromagnetic force. *J Mater Process Technol* 273:116247. <https://doi.org/10.1016/j.jmatprotec.2019.05.028>
10. Zhu Z, Ma X, Wang C, Mi G (2020) Altering morphological, crystalline and compositional features in 316 L laser-MIG weldments with an external magnetic field. *Mater Des* 196:109156. <https://doi.org/10.1016/j.matdes.2020.109156>
11. Xu L, Tang X, Zhang R, Lu F, Cui H (2021) Weld bead characteristics for full-penetration laser welding of aluminum alloy under electromagnetic field support. *J Mater Process Technol* 288: 116896. <https://doi.org/10.1016/j.jmatprotec.2020.116896>
12. Üstündağ Ö, Bakır N, Gumenyuk A, Rethmeier M (2021) Influence of oscillating magnetic field on the keyhole stability in deep

- penetration laser beam welding. *Opt Laser Technol* 135:106715. <https://doi.org/10.1016/j.optlastec.2020.106715>
13. Li J, Liu Y, Kang K, Sun Q, Jin P, Liu Y, Cai C, Sun Q (2021) A novel approach to regulate energy allocation and melt flow in narrow gap laser welding with electromagnetic assisted wire wobbling. *J Mater Process Technol* 289:116909. <https://doi.org/10.1016/j.jmatprotec.2020.116909>
  14. Cao L, Zhou Q, Liu H, Li J, Wang S (2020) Mechanism investigation of the influence of the magnetic field on the molten pool behavior during laser welding of aluminum alloy. *Int J Heat Mass Transf* 162:120390. <https://doi.org/10.1016/j.ijheatmasstransfer.2020.120390>
  15. Liu F, Tan C, Wu L, Gong X, Chen B, Song X, Zhao H, Wang G (2020) Influence of waveforms on Laser-MIG hybrid welding characteristics of 5052 aluminum alloy assisted by magnetic field. *Opt Laser Technol* 132:106508. <https://doi.org/10.1016/j.optlastec.2020.106508>
  16. Chen R, Kong HJ, Luan JH, Wang AD, Jiang P, Liu CT (2020) Effect of external applied magnetic field on microstructures and mechanical properties of laser welding joint of medium-Mn nanostructured steel. *Mater Sci Eng A* 792:139787. <https://doi.org/10.1016/j.msea.2020.139787>
  17. Gatzen M, Tang Z (2010) CFD-based model for melt flow in laser beam welding of aluminium with coaxial magnetic field. *Phys Procedia* 5:317–326
  18. Bachmann M, Avilov V, Gumenyuk A, Rethmeier M (2013) About the influence of a steady magnetic field on weld pool dynamics in partial penetration high power laser beam welding of thick aluminium parts. *Int J Heat Mass Transf* 60:309–321. <https://doi.org/10.1016/j.ijheatmasstransfer.2013.01.015>
  19. Bachmann M, Avilov V, Gumenyuk A, Rethmeier M (2016) Numerical assessment and experimental verification of the influence of the Hartmann effect in laser beam welding processes by steady magnetic fields. *Int J Therm Sci* 101:24–34. <https://doi.org/10.1016/j.ijthermalsci.2015.10.030>
  20. Rong Y, Huang Y, Xu J, Zheng H, Zhang G (2017) Numerical simulation and experiment analysis of angular distortion and residual stress in hybrid laser-magnetic welding. *J Mater Process Technol* 245:270–277. <https://doi.org/10.1016/j.jmatprotec.2017.02.031>
  21. Chen J, Wei Y, Zhan X, Gu C, Zhao X (2018) Thermoelectric currents and thermoelectric-magnetic effects in full-penetration laser beam welding of aluminum alloy with magnetic field support. *Int J Heat Mass Transf* 127:332–344. <https://doi.org/10.1016/j.ijheatmasstransfer.2018.08.004>
  22. Fuhrich T, Berger P, Hügel H (2001) Marangoni effect in laser deep penetration welding of steel. *J Laser Appl* 13:178–186. <https://doi.org/10.2351/1.1404412>
  23. Mills KC, Keene BJ, Brooks RF, Shirali A (1998) Marangoni effects in welding. *Philos Trans R Soc A Math Phys Eng Sci* 356: 911–925. <https://doi.org/10.1098/rsta.1998.0196>
  24. Zhang X, Zhao Z, Mi G, Wang C, Li R, Hu X (2017) Effect of external longitudinal magnetic field on arc plasma characteristics and droplet transfer during laser-MIG hybrid welding. *Int J Adv Manuf Technol* 92:2185–2195. <https://doi.org/10.1007/s00170-017-0293-2>
  25. Wang Z, Oliveira JP, Zeng Z, Bu X, Peng B, Shao X (2019) Laser beam oscillating welding of 5A06 aluminum alloys: microstructure, porosity and mechanical properties. *Opt Laser Technol* 111:58–65. <https://doi.org/10.1016/j.optlastec.2018.09.036>
  26. Wang H, Xu Y, Zheng H, Zhou W, Ren N, Ren X, Li T (2019) Monitoring and analysis of millisecond laser drilling process and performance with and without longitudinal magnetic assistance and/or assist gas. *J Manuf Process* 48:297–312. <https://doi.org/10.1016/j.jmapro.2019.10.015>
  27. Huang L, Liu P, Zhu S, Hua X, Dong S (2020) Experimental research on formation mechanism of porosity in magnetic field assisted laser welding of steel. *J Manuf Process* 50:596–602. <https://doi.org/10.1016/j.jmapro.2020.01.007>

**Publisher's note** Springer Nature remains neutral with regard to jurisdictional claims in published maps and institutional affiliations.